Transport and Sensing in Nanofluidic Devices

Kaimeng Zhou, John M. Perry, and Stephen C. Jacobson

Department of Chemistry, Indiana University, Bloomington, Indiana 47405-7102; email: jacobson@indiana.edu

Annu. Rev. Anal. Chem. 2011. 4:321–41

First published online as a Review in Advance on March 29, 2011

The *Annual Review of Analytical Chemistry* is online at anchem.annualreviews.org

This article's doi: 10.1146/annurev-anchem-061010-113938

1936-1327/11/0719-0321$20.00

Keywords

nanopore, nanochannel, ion-current rectification, resistive-pulse sensing

Abstract

Ion transport and sensing in nanofluidic devices are receiving a great deal of attention because of their unique transport properties and potential analytical applications. Some aspects of microscale transport transfer directly to the nanoscale, but nanofluidic systems can be significantly influenced by phenomena such as double-layer overlap, surface charge, ion-current rectification, diffusion, and entropic forces, which are either insignificant or absent in larger microchannels. Micro- and nanofabrication techniques create features with a wide range of well-defined geometries and dimensions in synthetic and solid-state substrates. Moreover, these techniques permit coupling of multiple nano- and microscale elements, which can execute various functions. We discuss basic nanofluidic architectures, material transport properties through single and multiple nanochannels, and characterization of single particles by resistive-pulse sensing.

1. INTRODUCTION

Resistive-pulse sensing: measurement of a change in ion current that results from a particle passing through an electrically biased pore filled with electrolyte

***I–V*:** current–voltage

Rectification ratio: absolute value of the ratio of the ion current measured at two applied potentials of equal magnitude but opposite sign

Recent advances in micro- and nanofabrication techniques have created opportunities to design increasingly sophisticated micro- and nanofluidic systems that have considerable potential for various analytical applications (1). The ability to design structures with nanometer dimensions, and to modify materials at the molecular level, benefits chemical analysis. Precise manipulation of fluids and analytes at the nanometer regime is critical in most nanofluidic devices, and thus, understanding what governs fluid behavior and material transport at the molecular scale is essential. In this review, we discuss basic nanofluidic architectures, the transport and active control of ions through these nanochannels, and a few examples of nanopore-based resistive-pulse sensing.

The two most common geometries for nanofluidic channels are symmetric and asymmetric nanochannels (**Figure 1**). Both types of nanochannels have a characteristic lateral dimension, such as diameter, width, or depth, on the nanoscale. For the symmetric channel (or cylindrical pore), ion transport through the channel is uniform in each direction, but as discussed below, the presence of surface charge can lead to enhanced counterion flux relative to coion flux. The asymmetric channel (or conical pore) has a geometrical asymmetry along the axis of ion-current flow that results from different dimensions between the tip (nanometer scale) and base (nanometer-to-micrometer scale). For an asymmetric channel, the magnitude of the ion current depends on whether counterions, such as the cations shown in **Figure 1*b***, travel from tip to base or from base to tip. When a potential is applied across the channel such that counterions travel from tip to base, the resulting ion current is higher than when counterion transport is from base to tip. These transport effects are typically studied by current–voltage (*I–V*) curves, and the degree of rectification (also known as the rectification ratio) is calculated by taking the absolute value of the ratio of the ion current measured at two applied potentials of equal magnitude but opposite sign.

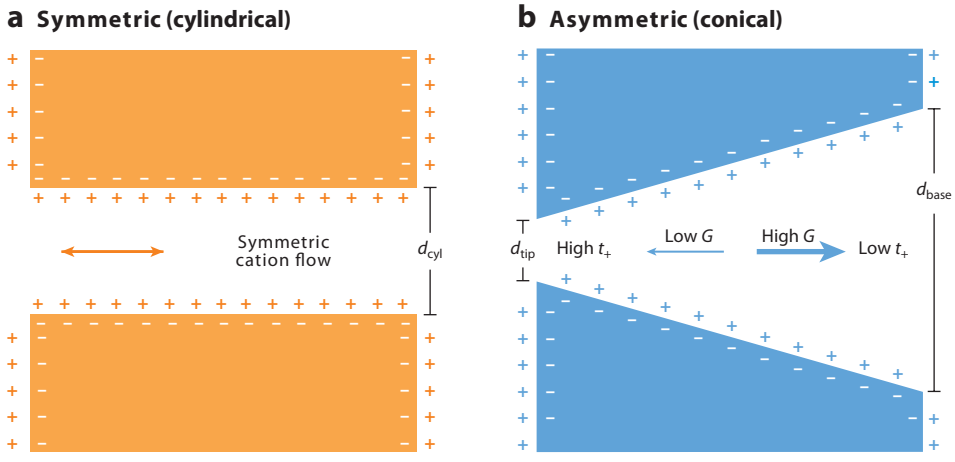

Figure 1

Schematics of symmetric (cylindrical) and asymmetric (conical) nanochannels with negative surface charge. (*a*) In a symmetric nanochannel, counterion (cation) transport does not depend on the polarity of the applied bias. (*b*) In an asymmetric nanochannel, the counterion transport depends on the polarity of the applied bias. Arrows show the direction of cation flux in high- and low-conductance (*G*) states, and the regions of high and low cation transference number (t_+) are indicated. d_{cyl}, d_{tip}, and d_{base} are the diameters of the cylinder, tip, and base, respectively. Panel *b* is adapted with permission from Reference 27. Copyright 2009, American Chemical Society.

2. NANOFABRICATION AND STRUCTURE DESIGNS

The two general categories of nanofluidic structures are nanopores and nanochannels, and these terms can be used interchangeably to describe similar systems. Nanopores are usually formed perpendicularly through the substrate plane, have a cylindrical or conical geometry, and are circularly symmetric along the pore length. Nanochannels are typically fabricated in the plane of a substrate, have lateral dimensions of depth and width, and are not circularly symmetric along the channel axis.

The nanopore category includes, for example, engineered protein pores (2), ion beam–sculpted pores (3), femtosecond laser–drilled pores (4), electron beam (*e*-beam)–drilled pores (5), nanopipettes (6), and track-etched synthetic nanopores (7). Compared with nanochannels, nanopores are formed in a greater variety of materials and have smaller lateral dimensions (e.g., 1–2 nm). The primary drawback is that such pores are more difficult to integrate into more complex devices that contain other nano- and microfluidic elements. **Figure 2*a*** shows a scanning electron microscope (SEM) image of a membrane with a track-etched conical pore with a tip diameter of 50 nm and a base diameter of 600 nm. More precise control of pore dimensions is obtained by milling pores with a focused ion beam or an *e*-beam. **Figure 2*b*** shows a transmission electron microscope (TEM) image of a 15-nm nanopore created in a 30-nm-thick silicon nitride membrane. This fabrication technique is used to form pores with diameters as small as 3 nm in membranes (5). Other thin-film materials, including graphene (8, 9), are used to make resistive-pulse sensors.

Membranes with track-etched pores have been incorporated into microfluidic platforms to form integrated devices with a single pore in the channel intersection (10). The pore density and channel width determine the number of pores in the device intersection, and each variable is controlled independently to match the desired experiment. Devices with multiple nanopores in the channel intersection are used for the electrophoretic and dielectrophoretic trapping of nanoparticles and cells (11), and similar multilayer structures with membrane interconnections are used to control sample dispensing in microfluidic separation systems (12, 13).

Nanochannels involve the fabrication of nanoscale patterns in a planar format. Various conventional micro- and nanofabrication techniques are used to create structures that are confined to the nanometer scale in one or two dimensions, such as sacrificial layer deposition (14), photolithography of nanoscale-depth microchannels (15, 16), and *e*-beam lithography (17, 18). For the first two methods, the channel depth is controlled down to nanometer dimensions, whereas focused ion-beam and *e*-beam techniques also confine the channel width to nanometer dimensions. In addition, ion- and *e*-beam writing permits any arbitrary two-dimensional geometry to be created. For example, nanochannels shaped as funnels with a narrow tip and wide base are easily formed in a planar format. **Figure 2*c*** shows SEM images of nanofluidic funnels with taper angles of 5°, 10°, and 20° and a straight channel (18). These funnels are cast in high-modulus poly(dimethylsiloxane) (h-PDMS) from masters written in the negative tone resist SU-8 by *e*-beam lithography. Ion transport through these channels is discussed below. More recently, sub-10-nm-wide nanochannels with lateral dimensions of less than 10 nm were formed by a self-sealing and seal-limiting atomic layer–deposition method (19). Another fabrication technique creates a simple nanoscale gap between microchannels in PDMS by breaking down the junction between adjacent channels with an electric field (20). However, dimensional control with this method is more difficult. Two primary advantages of fabricating nanofluidic channels in the plane of the substrate are (*a*) integration into more complex devices and (*b*) the ability to image material transport optically, which helps with understanding transport mechanisms.

3. ION TRANSPORT

A thorough understanding of ion-transport mechanisms and electrical properties of the nanochannels is required to fully exploit potential applications with nanofluidic devices. As

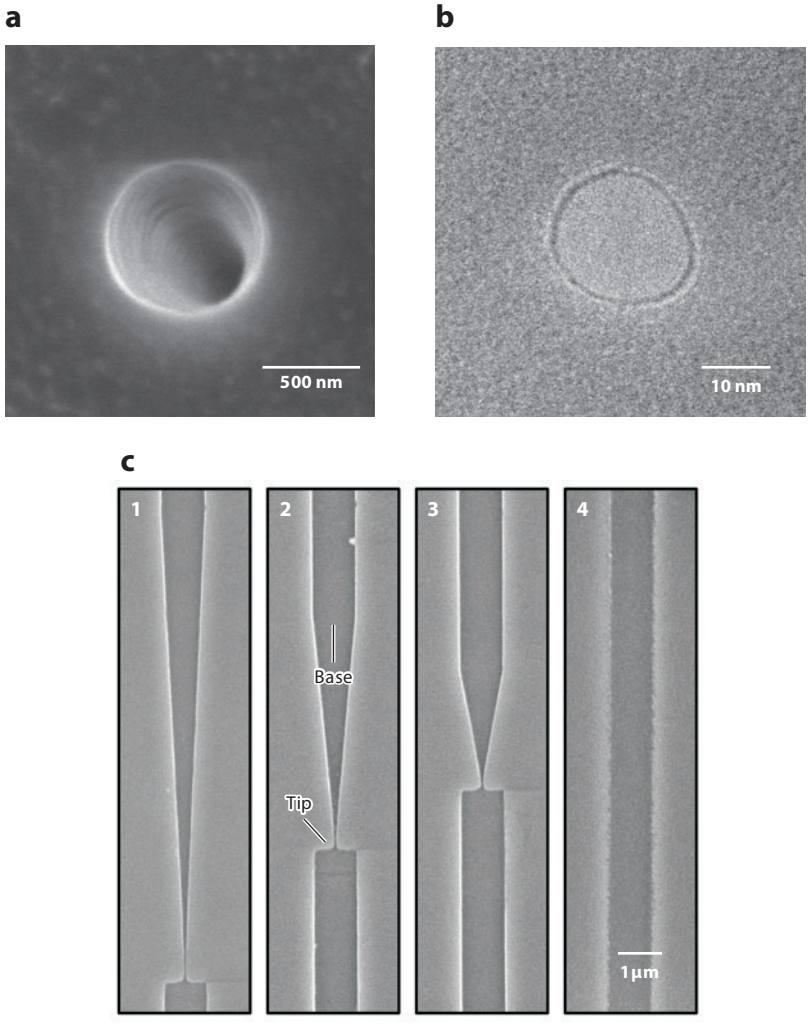

Figure 2

A conical track-etched nanopore, a cylindrical nanopore in silicon nitride, and in-plane nanofluidic funnels. (*a*) Scanning electron microscope image of the base of a conical nanopore etched in a poly(ethylene terephthalate) membrane. The tip diameter is 50 nm, and the base diameter is 600 nm. (*b*) Transmission electron microscope image of a cylindrical nanopore drilled into a 50-nm-thick silicon nitride membrane. The pore diameter is 15 nm. (*c*) Nanofunnels with (*1*) 5°, (*2*) 10°, and (*3*) 20° taper angles and (*4*) a straight nanochannel cast in high-modulus poly(dimethylsiloxane) from SU-8 masters created by electron-beam lithography. The funnel tips are 80 nm wide and 120 nm deep. Panel *c* is adapted with permission from Reference 18. Copyright 2010, American Chemical Society.

channel dimensions shrink from micrometers to nanometers, phenomena such as double-layer overlap, ion permittivity, diffusion, surface charge, and entropy, which are negligible or absent in microchannels, play an increasingly important role (21, 22). In this section, we discuss what channel characteristics influence ion-current rectification and how surface charge leads to ion enrichment and depletion. In turn, nanofluidic diodes and transistors are used to control fluidic behavior.

3.1. Ion-Current Rectification

When an asymmetry exists in the geometry, surface charge, or buffer system of a nanochannel, ion-current rectification can occur. Ion-current rectification stems from ion-current flux that is higher in one direction than in the other, and the rectification ratio describes the degree of rectification. Current rectification was first reported in a quartz nanopipette electrode (6), and subsequently, rectification has been observed in silicon nanochannels (23), track-etched polymer nanopores (24), and h-PDMS nanofunnels (18).

A 5° tapered funnel with an 80-nm-wide tip fabricated in h-PDMS exhibits higher current rectification than do funnels with 10° and 20° tapers. Because the funnels have similar surface-to-volume ratios and surface chemistries, the taper angle and surface area contribute to rectification. **Figure 3*a*** compares the *I–V* curves for a 5° funnel and a straight channel. The straight nanochannel displays ohmic behavior, and the current is linear with applied potential. The 5° funnel, however, exhibits ion-current rectification in which the funnel is in a high-conductance state at negative applied potentials and in a low-conductance state at positive potentials. In this example, the potential at the funnel base is varied, and the funnel tip is held at ground. Current rectification in nanofluidic channels is somewhat different from what is observed when an electronic diode is forward- or reverse-biased. Most notably, when an electronic diode is reverse-biased, the measured current is negligible, whereas a nanofluidic diode can exhibit a nonnegligible current when reverse-biased.

Electrolytes with lower ionic strengths typically generate stronger ion-current rectification (25) because the surface charge contributes more to the total ion current (26, 27), and this contribution is determined by measuring channel conductivities over a range of ionic strengths. **Figure 3*b*** shows that the conductivities for the 5° funnel and the straight channel are almost identical to bulk conductivities at high ionic strength but deviate from bulk conductivities at low ionic strength.

Double-layer overlap: when the electrical double-layer thickness is greater than or equal to the smaller lateral dimension of a fluidic channel

Ion-current rectification: state in which ion current in an electrically biased channel is larger in one direction than the other

Diode: a two-terminal component that preferentially conducts current in one direction

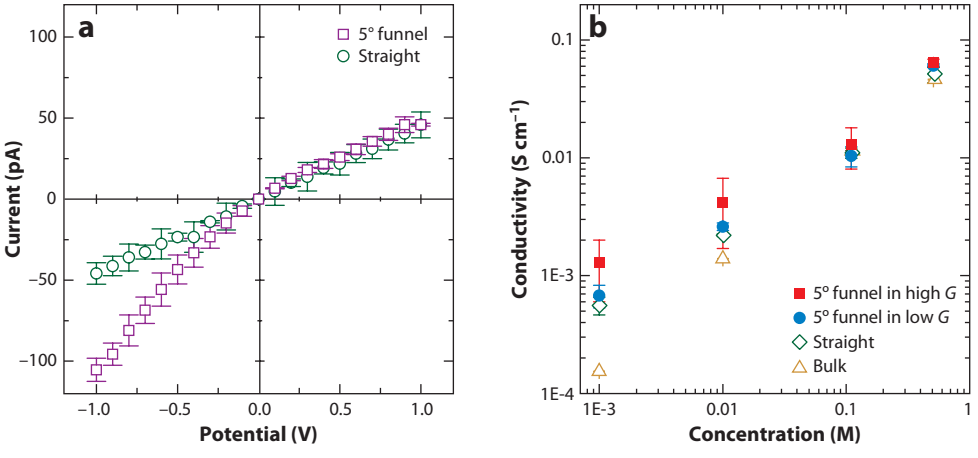

Figure 3

Ion-current rectification in nanofunnels. (*a*) Current–voltage curves for 5° funnels and straight channels filled with 1 mM potassium phosphate buffer (pH 6.7). The potential was applied to the base with the tip grounded. (*b*) Variation of the conductivity with buffer concentration for 5° funnels in the low- and high-conductance (*G*) states, straight channels, and bulk buffer. See **Figure 2*c*** for scanning electron microscope images of the 5° funnel and straight channel. Adapted with permission from Reference 18. Copyright 2010, American Chemical Society.

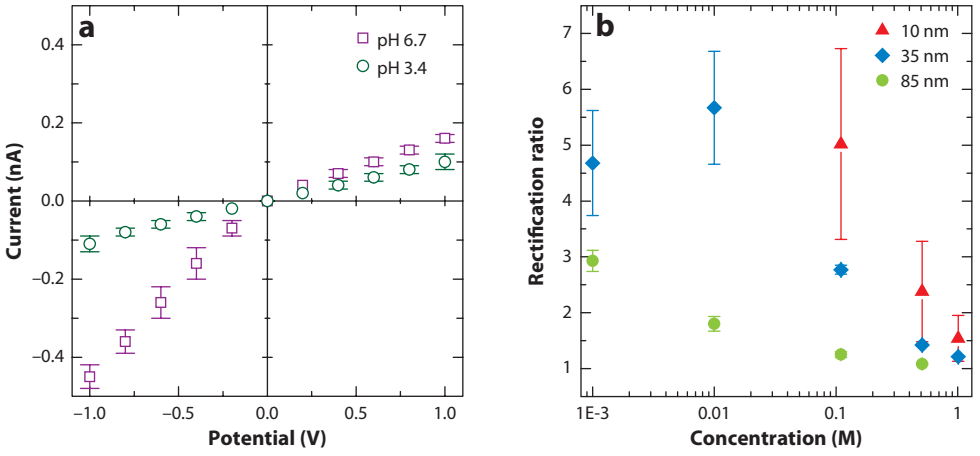

Figure 4

Ion-current rectification in conical nanopores. (*a*) Current–voltage curves for a conical pore with an 85-nm-diameter tip filled with 1 mM potassium phosphate buffer (pH 6.7) and 1 mM sodium acetate buffer (pH 3.4). (*b*) Variation of rectification ratio with phosphate buffer concentration (pH 6.7) for the 10-, 35-, and 85-nm pores. The rectification ratio is the absolute value of the current measured at −1 V divided by the current measured at +1 V. See **Figure 2*a*** for a scanning electron microscope image of a conical track-etched pore. Adapted with permission from Reference 27. Copyright 2009, American Chemical Society.

The high-conductance state also exhibits a higher conductivity than the low-conductance state for the funnels, whose conductivity is comparable to that of the straight channel.

Current rectification is a surface-driven phenomenon and, consequently, is altered by surface modification (28) or by adjustment of the buffer pH (24, 29). In the case of a conical pore in a poly(ethylene terephthalate) (PET) membrane, the isoelectric point of the carboxylate groups on the pore wall is ∼3.7 (30). As a result, when an acetate buffer of pH 3.4 is used, the *I–V* curve shows no current rectification (**Figure 4*a***). In contrast, when a phosphate buffer of pH 6.7 is used, current rectification is observed because the carboxylate groups are deprotonated, and the net surface charge in the pore is negative. **Figure 4*a*** compares *I–V* curves for a conical pore with an 85-nm-diameter tip that rectifies current at pH 6.7 but not at pH 3.4.

Pore dimensions are also critical parameters for current rectification. Generally, the rectification ratio decreases with increasing tip diameter (27), and only a few experimental results show current rectification with pore diameters ≥50 nm (15, 31, 32). **Figure 4*b*** shows the variation of the rectification ratio for conical pores with tip diameters of 10, 35, and 85 nm. The smallest (10-nm-diameter tip) pores in this study show the highest rectification ratio at all ionic strengths, whereas the largest (85-nm-diameter tip) pores exhibit the lowest rectification ratio. Interestingly, the 35-nm pores have a maximum rectification ratio at a buffer concentration of 10 mM. In addition, double-layer thickness increases with decreasing ionic strength. As a result, double-layer overlap may occur for smaller-diameter pores at lower ionic strengths, resulting in enhanced rectification (33).

3.2. Modeling of Ion Transport

PET: poly(ethylene terephthalate)

Although numerous studies have investigated the rectification process, the exact mechanism is still under debate (34). Initially, a ratchet model suggested that a potential well is formed upon the combination of applied bias and the potential that arises from the surface charge on the pore

wall when the pore tip dimension is comparable to the double-layer thickness (28). Simulations of the electric field along the pore have confirmed the presence of this potential well (35). However, the magnitude strongly depends on the surface-charge density and applied potential (33, 36). In this model, when the working electrode is at the base side and the applied potential is positive, counterions (cations) become trapped in the potential well as they travel through the pore, which results in lowered conductivity. However, when the electrical bias is reversed, the potential well is significantly smaller, which results in enhanced nanopore conductivity.

Transference number: the fraction of the total current that is carried through an electrolyte solution by a specific type of ion

Another model is based on the difference in cation transference number along the pore and the resulting ion depletion and enrichment inside the nanopore (37). This model is predicted by numerical simulation with the Poisson–Nernst–Planck system of equations (25, 33, 35, 36, 38). Due to the conical shape of the nanopore, a higher surface-to-volume ratio is expected at the pore tip compared with the rest of the pore, which suggests a higher counterion transference number at the tip and a lower counterion transference number at the base. When a potential is applied so that counterions travel from base to tip, a depletion region is formed at the tip because the counterions are not replenished quickly enough, which leads to a low-conductance state. Conversely, as counterions travel from tip to base, counterion enrichment occurs within the nanopore, which results in a high-conductance state. Despite these differences, both mechanisms suggest two major criteria for current rectification: (*a*) an asymmetry in the surface-charge profile along the current flow and (*b*) a channel dimension that is sufficiently small.

Theoretical modeling also examines how specific geometries, such as bullet-like, trumpet-like, and hybrid-shaped nanopores, affect current rectification (39). In these simulations, the bullet-shaped nanostructures exhibit greater rectification compared with conical, trumpet-like, or hybrid-shaped pores. This finding may explain the recent observation that nanopores with very large (e.g., 380-nm) tip diameters exhibit diode-like rectification behavior (27) and demonstrates the possibility of producing rectification at a larger scale, which may have the benefit of easier and less expensive fabrication. Cylindrical nanopores that connect two pores with micrometer diameters also rectify ion current due to asymmetric concentration polarization (31).

More recent work demonstrates that electroosmotic flow is used to generate current rectification even in pores with micrometer dimensions (40). Theoretical work confirms this finding and shows that the contribution of electroosmotic flow becomes more significant with higher applied potential and intermediate or higher values of (*a*) the tip radius divided by double-layer thickness and (*b*) surface-charge density (41).

3.3. Ion Enrichment and Depletion

Other phenomena that take place in nanofluidic systems are ion enrichment and depletion, which occur at the nano- and microfluidic interface (21). Unlike current rectification, these phenomena do not require surface-charge asymmetry along the channel but arise from the high surface-to-volume ratio of the channels and the preferential transport of the counterions (10, 26).

When a potential is applied across the channel, an unbalanced ion flux occurs with or without the presence of double-layer overlap (**Figure 5*a***). With double-layer overlap, the channel is ion permselective (42). Coions (e.g., anions if the surface is negatively charged) are repelled from the charged surface and do not readily enter the channel. Counterions (cations), however, migrate freely through the channel, which results in concentration polarization (43). When diffusive transport is slower than the electrophoretic transport of ions, cations are depleted on the anodic side of the channel and concentrated on the cathodic side. If electrical neutrality in the lateral direction is assumed, the anion concentration mimics the cation concentration. Without double-layer

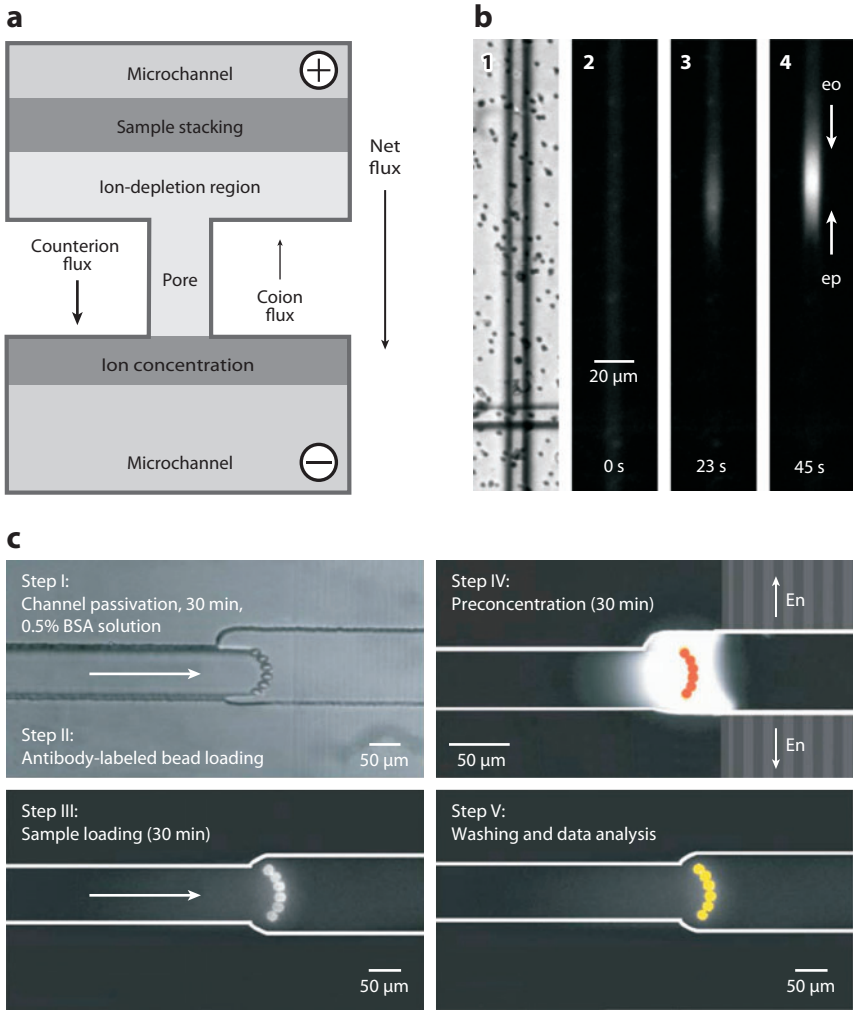

Figure 5

Ion enrichment and depletion at nanochannel–microchannel interfaces. (*a*) Ion enrichment, depletion, and sample stacking resulting from the unbalanced ion flux across the nanochannel. (*b*) (*1*) Transmitted light image of the microfluidic device with a single nanopore isolated in the channel intersection. (*2–4*) Fluorescence images of fluorescein stacking at (*2*) 0 s, (*3*) 23 s, and (*4*) 45 s after application of 5 V. Arrows show the direction of electroosmotic (eo) and electrophoretic (ep) transport. Adapted with permission from Reference 10. Copyright 2008, American Chemical Society. (*c*) The bead-loading, immunosensing, and preconcentration procedure used to enhance sensitivity and the detection dynamic range for a bead-based immunoassay. Abbreviation: BSA, bovine serum albumin. Reproduced from Reference 47 with permission from the Royal Society of Chemistry.

overlap, concentration polarization arises from enhanced cation transport caused by the surface charge rather than from hindrance of anion transport.

In addition, samples stack at the boundary of the depletion region on the anodic side when the electroosmotic and electrophoretic forces are balanced (**Figure 5*b***) (10). At low applied potentials, diffusion dominates, and concentration polarization does not arise. In contrast, at high

applied potentials, concentration boundaries may not be stable because of fluid vortices, which are caused by nonequilibrium electroosmotic flow and are observed both optically and electrically (44). Experimental results, combined with computational models, suggest that the width and propagation velocity of the concentration polarization zone scale with the square root of time at constant voltage (45).

Applications of the enrichment process include millionfold preconcentration of proteins, which is achieved within 40 min with a nanochannel filter coupled to microchannels (46). This concentration process is promising for sample preparation and detection and is especially useful for analysis of biological samples present at low concentrations. In such analyses, biomolecules are preconcentrated at an interface between deep and shallow channels, where streptavidin-coated polystyrene beads with antibodies are trapped to enhance immunoassay sensitivity and detection dynamic range (**Figure 5*c***) (47). Simultaneous enrichment and separation are achieved through modulation of the potential applied to a bipolar electrode in a microfluidic channel (48). In this case, molecules with different electrophoretic mobilities are focused in different zones, and up-to-600-fold enhancements are accomplished within 400 s. In addition, seawater is desalinated on microfluidic devices by ion-concentration polarization (49). Water molecules enter a microchannel with an ion-depletion zone, whereas charged species such as salts are excluded and pushed into another microchannel without an ion-depletion zone.

3.4. Nanofluidic Diodes and Transistors

As discussed above, nanochannels with an asymmetry along the axis of current flow can rectify current. Numerous methods to modify surface chemistry or channel geometry have been explored in attempts to enhance the rectification ratio and improve diode-like *I–V* behavior. The ability to precisely modulate ion transport in such channels permits the design and fabrication of application-specific circuits composed of fluidic diodes and transistors. In several examples, the *I–V* characteristics of these diodes and transistors are similar to their electronic counterparts.

Early studies in surface modification show that ion transport is controlled by attaching thiolated DNA molecules onto gold-coated conical nanopores (50). Depending on the polarity of the applied potential, the DNA molecules are either directed into the pore, physically impeding ion flow, or forced out of the pore, allowing greater ion flux. Little to no rectification is observed when shorter DNA molecules (12-mers) are immobilized on the pore surface; the on and off states of the diode are more pronounced when longer DNA molecules (45-mers) are attached (**Figure 6**). In another example, layer-by-layer deposition of polyelectrolytes, such as poly(allylamine hydrochloride) and poly(styrenesulfonate), in a conical PET pore demonstrates that the degree of rectification is tuned via surface modification (41). Another approach is to modify the channel surface with pH-responsive polymer brushes. Attachment of zwitterionic brushes [poly(methacryoyl-L-lysine)] onto a pore formed in a polyimide membrane (51) allows ion transport not only to be controlled between the on and off states but also to be switched by tuning the buffer pH. Surface modification with other pH-responsive polymer brushes [e.g., poly (4-vinyl-pyridine)] (52) produces diode-like *I–V* behavior. At basic pH, the polymer brushes become hydrophobic and neutral and collapse inside the pore, allowing ion current to pass. At acidic pH, the brushes are charged and hydrophilic and extend into the pore, thereby blocking ion transport.

Introduction of a discontinuous surface charge in the channel is also a viable way to produce asymmetries. In one example, biotin is used to functionalize the entire channel surface, and bands of labeled and unlabeled streptavidin are bound to the channel surface by a diffusion-limited patterning method (53). Similarly, a concentration gradient is created by placing the reagent on only one side of the pore to selectively modify the pore tip. The resulting rectification ratio goes

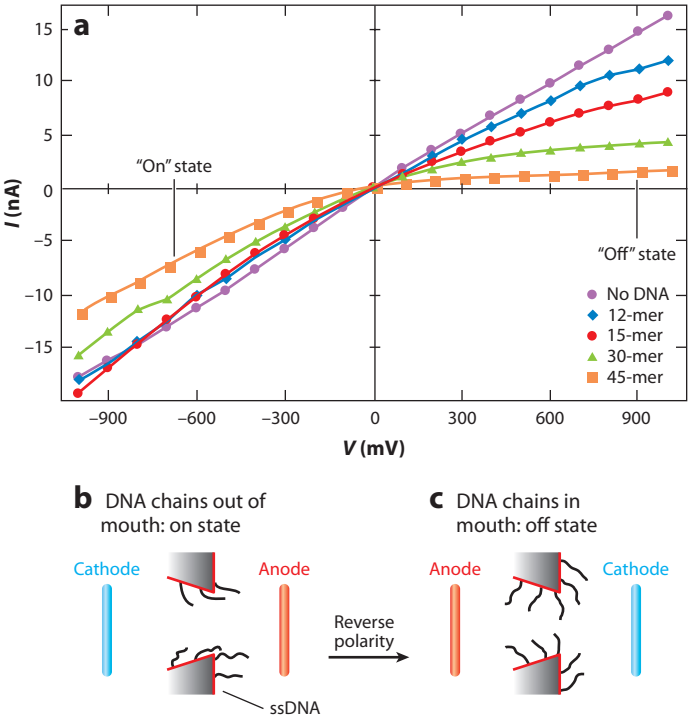

Figure 6

DNA–nanopore artificial ion channel. (*a*) Current–voltage (*I–V*) curves for conical track-etched pores with no DNA and with 12-mer, 15-mer, 30-mer, and 45-mer DNA strands attached to the pore wall. The tip diameter is 40 nm. Also shown are electrode polarity and DNA-chain positions for the (*b*) on and (*c*) off states. Abbreviation: ssDNA, single-stranded DNA. Reprinted with permission from Reference 50. Copyright 2004, American Chemical Society.

up to hundreds, with an applied potential from −5 V to +5 V (54). Recently, a SiO_2-Al_2O_3 heterostructured nanotube was fabricated by combining atomic layer deposition and selective etching on a silicon nanowire as a template (55). This fabrication method produces a structure with two distinct surface charges that is tuned by pH and has diode-like rectification at ionic strengths less than 3 mM.

Following the advent of diodes, the next step is to develop a fluidic transistor that permits a higher degree of control over ion and fluid transport. Development of efficient nanofluidic transistors may eventually lead to fluidic logic operations or large-scale nanofluidic circuits. Most transistor-like devices rely on changing the local surface charge in the structure by applying an external field. In a three-terminal device (e.g., composed of a source, drain, and gate), the gate potential modulates the ion current in the channel, thereby allowing control of ion transport within the device (56–58). In a channel with negative surface charge, a negative gate potential produces cation enrichment at the junction of the external electrode and increases the channel conductance. A positive gate potential has the opposite effect. Simulations show that this gating effect occurs even when the channel dimensions are not comparable to the double-layer thickness (59). Nanofluidic transistors influence the transport properties of ions ranging in size from dyes (60) to DNA (56).

Nonlinear ion transport is observed in nanofluidic transistors when source-drain biases greater than 5 V are applied and hydrodynamic slip is induced by the applied field (61). Such experiments

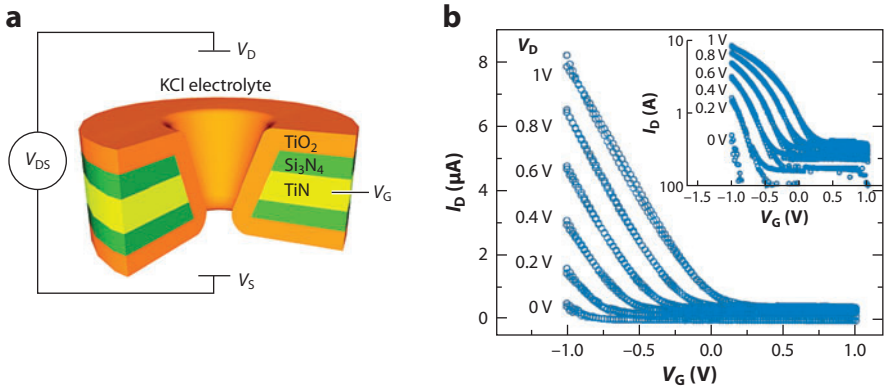

Figure 7

Ionic field-effect transistor formed from electrode-embedded nanopores. (*a*) Ionic transport through the nanopores is manipulated by application of a potential to the gate electrode (TiN), which is surrounded by a gate dielectric (TiO_2) and Si_3N_4 layers. (*b*) Variation of drain current (I_D) with gate potential (V_G) for various drain potentials (V_D = 0–1 V). *p*-Type unipolar behavior suggests that the majority carrier consists of K^+ ions. The inset in panel *b* is the log plot of I_D versus V_G. Adapted with permission from Reference 62. Copyright 2009, American Chemical Society.

require a sufficiently low ionic strength for which the double-layer thickness exceeds the channel width and, as a result, channel conductance increases by 20- to 50-fold. Another way to integrate the gate electrode in a multipore system is shown in **Figure 7** (62). After pores are formed by *e*-beam lithography and reactive ion etching, atomic layer deposition is used to fabricate the gate electrode as well as narrow the pore diameter. **Figure 7*b*** shows that the ionic conductivity of the nanopore is effectively modulated by the gate potential, V_G. The ionic current increases with a negative gate potential, whereas a positive gate potential has little influence on the conductivity. The unipolar behavior is analogous to that of a *p*-type field-effect transistor (FET), suggesting that the majority carrier is the counterion. The above transistor examples use an electrode that is external to the fluidic channels to manipulate ion transport; they are the microfluidic equivalent of FETs. An alternative design is to couple three funnels (**Figure 2*c***) together in a planar device, which is more similar to a bipolar junction transistor. **Figure 8*a*** shows a three-terminal structure composed of three 5° funnels whose tips point inward toward the center of the device (referred to as the 3-in transistor device). The funnel tips can point inward or outward, and the applied potentials are configured to create high- or low-conductance states for each funnel. These devices easily enrich or deplete samples in the center of the device (**Figure 8*b***).

3.5. Ogston Sieving and Entropy-Based Separation

Conventional separation techniques for proteins and nucleic acids, such as gel electrophoresis, are limited in resolution due to the irregular interactions between the molecules and the randomly oriented sieving matrix, which has a wide distribution of pore sizes. In contrast, the formation of a matrix with uniform, well-defined micro- and nanochannels provides fixed paths for separations. As the channel dimensions approach molecular length scales, increased entropic effects hinder analyte transport and lead to Ogston sieving (63) or entropy-based separations. Separation of DNA molecules of different lengths with nanopillar arrays (64) is achieved through the complete insertion of shorter DNA molecules and the partial insertion of longer DNA molecules into a

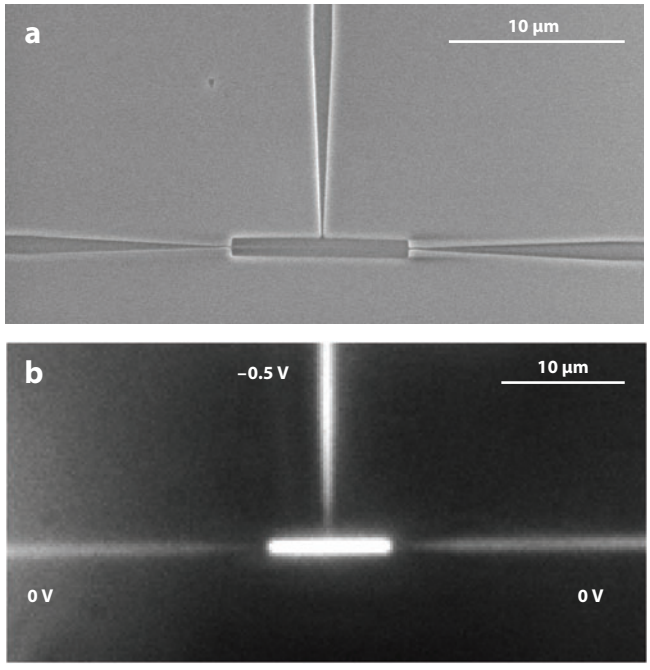

Figure 8

Nanofluidic transistor composed of three nanofunnels. (*a*) Scanning electron microscope image of a high-modulus poly(dimethylsiloxane) replica of an in-plane transistor with three nanofunnels whose tips are turned inward toward the center of the device (known as the 3-in transistor design). The funnel tips are 80 nm wide and 100 nm deep. (*b*) Fluorescence image of fluorescein enrichment in the center region of the 3-in transistor design. The applied potentials are listed.

region that is entropically unfavorable. Longer DNA molecules are allowed to relax and recoil back to their native state and, therefore, are separated from the shorter DNA molecules.

Structures with repeating deep (1.5–3-μm) and shallow (75–100-nm) channels allow efficient separation of DNA molecules ranging from 5,000 to 160,000 bp in length (65). The DNA molecules are trapped in the deep channel, where they must overcome the entropic energy barrier to enter the shallow region. The ability to escape the entropic trap depends on the local deformation of the molecules (66), whereas the activation energy is independent of the molecular size (67). If part of the molecule enters the shallow region, the entire DNA molecule is pulled through. Thus, larger DNA molecules with more surface area exposed to the shallow region have a higher probability of threading into the shallow region, which results in size-dependent separation.

In a recent study, two-dimensional sieving structures with alternating deep and shallow channels continuously separated biomolecules by Ogston sieving, entropic trapping, or electrostatic separation (16). When short DNA molecules (e.g., polymerase chain reaction markers) with a radius of gyration smaller than the depth of the shallow channels are analyzed, Ogston sieving dominates, and the larger molecules have lower observed mobilities and, therefore, smaller deflection angles. In contrast, when large DNA molecules are used as the sample, an entropy-based separation occurs, and the larger molecules have higher mobilities and, therefore, larger deflection angles. Such devices produce efficient biomolecular separations and directly probe the transition between Ogston sieving and entropic trapping.

4. RESISTIVE-PULSE SENSING

When nanochannels have lateral dimensions similar to the molecular dimensions of the analyte, these channels serve as single-molecule sensors (68). The basic sensing scheme relies on measuring ion-current changes as molecules or particles pass through an electrically biased channel. Counting these individual translocation events is referred to as resistive-pulse sensing (7) or Coulter counting. This detection method is rapid, label-free, and nondestructive and has been used to characterize various samples, including metal ions, small molecules, nanoparticles, DNA, proteins, viruses, and immune complexes. Further development of this technique may eventually permit nanopore-based DNA sequencing (69). In this section, we discuss nanopore sensors formed from different materials, the experimental conditions that affect the sensing quality, and physical models that describe the particle-transition process.

4.1. Biological Nanopores

Biological pores are highly reproducible in terms of their composition and dimensions. In an early example, resistive-pulse sensing was performed with a single alamethicin pore inserted into a lipid bilayer, in which poly(ethylene glycol) molecules with radii of gyration from 0.5 to 1.5 nm were detected (70). Later, an α-hemolysin (αHL) pore, which is a mushroom-shaped heptamer protein pore with an interior diameter ranging from 1.4 to 2.6 nm, was used for resistive-pulse sensing of nucleic acid molecules because of the well-defined structure of the pore (71). The protein pore is suspended in a lipid bilayer, which separates two fluidic chambers. By applying a potential across the pore, single-stranded DNA (ssDNA) and RNA are threaded through in a linear fashion. The presence of a molecule is detected by a temporal decrease in ionic conductance through the nanopore, and the current blockage events show that the transit time through the pore is proportional to the length of the polynucleotide molecules (72).

Biological pores, such as αHL, are also readily engineered to enhance analyte selectivity (73, 74). In one example, four histidines are engineered inside the pore wall to form a mutant subunit, and the subunit further interacts with six wild-type subunits to form a heteromeric pore, which binds specifically with divalent metal ions. Each binding event results in a change in pore conductivity, and nanomolar detection limits for Zn^{2+} are reported. However, there are drawbacks to biological pores. For instance, the pore structure is fixed and has a limited diameter range; also, such pores lack durability due to the fragile nature of the supporting lipid bilayers. The use of glass nanopore pipettes as a solid support of the lipid bilayer helps to address these stability issues (75, 76). Suspension of the lipid bilayers across a small (10–1,000-nm) opening significantly decreases the area of the lipid bilayer and, therefore, increases voltage stability, mechanical vibration resistance, and lifetime (77), which in turn improves the ion-recording quality of biological pores. **Figure 9** demonstrates multiple event sensing in a glass nanopore membrane with multiple αHL pores inserted. This example shows that multiple sensing events are easily discriminated by applying ac waveforms to sense binding events.

4.2. Solid-State Nanopores

Use of solid-state nanopores in resistive-pulse sensing intensified after an initial demonstration in which pores were formed in a silicon nitride membrane by ion-beam sculpting (3). *e*-Beam lithography and milling by transmission electron microscopy methods are alternative approaches to the fabrication of solid-state nanopores with single-nanometer dimensions (5). Solid-state nanopores are formed over a range of dimensions with well-defined geometries, are straightforward to

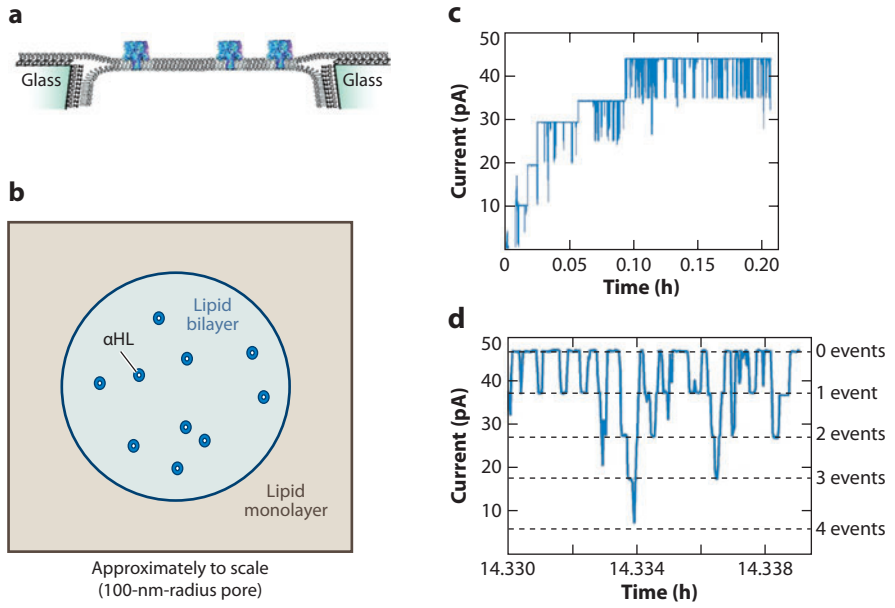

Figure 9

Multiple event sensing with ac waveforms. (*a*) Cross-sectional view of α-hemolysin (αHL) channels inserted into a lipid bilayer suspended over the small orifice of a glass nanopore pipette. (*b*) Top view showing multiple αHL channels (drawn approximately to scale). (*c*) Variation of ac current with time corresponding to multiple αHL channel insertions and heptakis-(6-*O*-sulfo)-β-cyclodextrin (s_7 βCD)-binding events. The initial 12 min with the first 4 αHL channel insertions are shown. (*d*) An ∼30-s segment in which the conductance states correspond to 0, 1, 2, 3, or 4 simultaneous s_7 βCD-binding events. These data were recorded with a 10-mV root-mean-square, 100-Hz ac signal superimposed on a −10-mV dc signal. Adapted with permission from Reference 76. Copyright 2008, American Chemical Society.

integrate into more complex devices, and exhibit excellent durability compared with biological nanopores (68, 78).

Numerous resistive-pulse sensing experiments with solid-state nanopores have focused on characterization of DNA translocation (79). When the nanopore diameter (3 nm) is slightly larger than the cross-sectional size of the molecule [2 nm for a 3-kbp double-stranded DNA (dsDNA)], a narrow distribution of pulse amplitudes (Δi) for translocation events is observed. This distribution indicates translocation in an unfolded state. However, when a 10-nm pore is used, the Δi distribution broadens. Multilevel events and large single-level events with a Δi that is twice as high as that of small single-level events are observed, suggesting that DNA molecules are in a folded state as they pass through the pore. An ultrasmall pore is not necessary to linearize DNA molecules because more than 50% of the events observed with the 10-nm pore appear to be unfolded translocation events (80).

Rapid discrimination between dsRNA and ssRNA with solid-state nanopores recently became possible (81). Translocation events for dsRNA have a larger change in conductance than do similar events for ssRNA at high applied potentials. One possible explanation for this finding is based on the difference in the flexibility between dsRNA and ssRNA. ssRNA is more flexible and is stretched more easily at high potentials; therefore, ssRNA occupies a smaller fraction of the pore space, which results in smaller change in pore conductance. Furthermore, solid-state nanopores

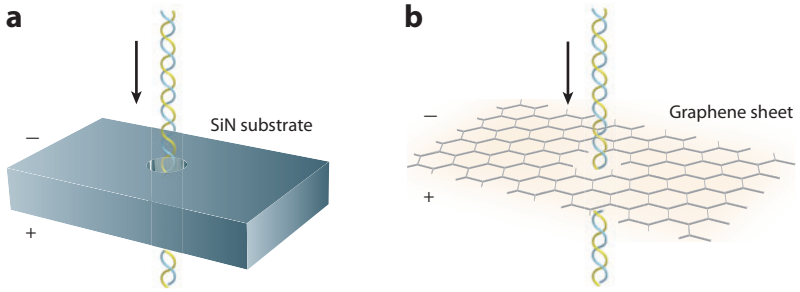

Figure 10

Schematics of DNA translocating through nanopores formed in a silicon nitride (SiN) film and graphene sheet. (*a*) The SiN film is ~30–50 nm thick. (*b*) The graphene sheet is ~0.5 nm thick.

characterize local structures along the length of DNA molecules such as RecA-coated DNA (82, 83), PNA-tagged DNA molecules (84), and DNA-binding molecules (85).

Research involving solid-state nanopore sensing shows potential for DNA sequencing. However, solid-state substrates, such as silicon, silicon dioxide, and silicon nitride, are limited in sensing resolution due to the length of the pore, that is, the thickness of the membrane in which the pore is formed. Recently, translocation of DNA through pores fabricated in graphene sheets that are one or two atomic layers thick was demonstrated (8, 9). The thin graphene layer (86) may dramatically increase the sensitivity for DNA profiling because the changes in conductance for individual bases may be resolved. **Figure 10** depicts DNA threading through pores formed in a silicon nitride membrane and a graphene sheet. The graphene sheet is 50–100 times thinner than the silicon nitride membrane and may permit single–base pair resolution for sequencing applications.

4.3. Synthetic Nanopores

As described above, synthetic nanopores fabricated in track-etched polymer membranes exhibit interesting ion-transport properties. Resistive-pulse sensing with similar pores includes detection of single porphyrin molecules with a conical pore formed in a polyimide film (87); such a pore has a 4.5-nm tip opening, which permits translocation of the 2-nm porphyrin molecules. In another example, 40-nm-diameter pores in polycarbonate membranes are used to characterize and discriminate double-stranded DNA and single-stranded DNA molecules (88). An advantage of synthetic nanopores is that the pore surface is easily modified. Gold is coated onto the interior surface of the pores by an electroless plating method (89), which allows functionalization of the surface with thiolated species and other chemicals that interact with gold. Thiolated biotin derivatives are attached to the pore surface following gold deposition, and binding of streptavidin molecules to the surface-bound biotins results in permanent blockage of the ion current (90). In addition, free bovine serum albumin molecules are distinguished from complexes formed by fragment antigen binding to bovine serum albumin (91). In this experiment, gold-coated pores are functionalized with poly(ethylene glycol)-thiol molecules to minimize nonspecific protein adsorption. A drawback to the track-etched pores is that etching of the pore to an exact dimension is somewhat difficult; however, the process is substantially improved by a two-step etching process (92).

Characterization of viruses (93), antibody–virus interactions (4), and immune complexes (94) is achieved by resistive-pulse sensing. For femtosecond laser–drilled pores in glass substrates, the pore diameters range from 575 to 900 nm and are used to sense virus complexes with diameters of 100 to 200 nm (4). Pulse amplitudes increase with time following the addition of antibodies,

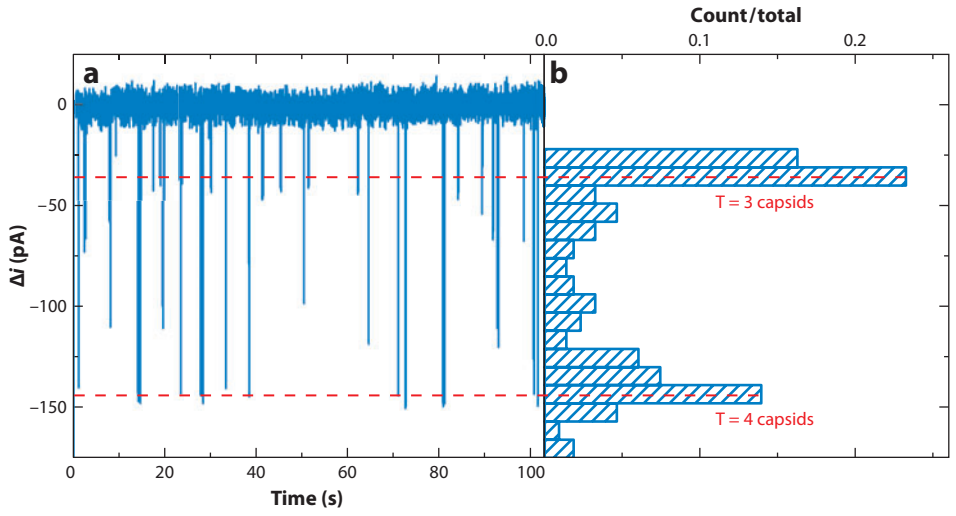

Figure 11

Characterization of hepatitis B virus (HBV) capsids by resistive-pulse sensing. (*a*) Variation of pulse amplitude (Δi) with time for a mixture of empty T = 3 and T = 4 HBV capsids analyzed with a track-etched conical nanopore (**Figure 2*a***). The tip diameter is 40 nm, and the applied potential is 0.3 V. Dashed lines indicate the current pulses for T = 3 and T = 4 capsids. (*b*) Histogram of Δi for the T = 3 and T = 4 capsids analyzed in panel *a*. There are 212 total counts, and the ratio of counts for the T = 3 and T = 4 capsids is 1.31. Adapted with permission from Reference 95. Copyright 2011, American Chemical Society.

and the number of antibodies bound to virus particles is calculated on the basis of changes in pulse amplitudes. Recently, hepatitis B virus capsids were characterized with conical pores formed in PET membranes (95). The tip diameters of the pores ranged from 40 to 50 nm, and the pore surface was covalently modified with triethylene glycol to minimize capsid adsorption and to suppress electroosmotic flow in the pore. Such nanopore devices easily discriminate between 3-MDa T = 3 capsids and 4-MDa T = 4 capsids, which are 31 nm and 36 nm in diameter, respectively. **Figure 11*a*** shows the difference in Δi for the T = 3 and T = 4 capsids. The icosahedral T = 3 and T = 4 capsids are nearly identical in chemical composition and surface charge per unit area. However, the large difference in transit time (Δt) between the T = 3 and T = 4 capsids suggests that an entropic barrier must be overcome to enter the pore. A similar phenomenon is observed for DNA translocation through solid-state pores (96). **Figure 11*b*** shows a histogram of Δi, and the ratio of counts for T = 3 and T = 4 capsids is 1.31, compared with the actual concentration ratio of 0.11. These data demonstrate that the nanopore favors the transport of the smaller, T = 3 capsids. These results agree well with a model that describes the partition coefficient of spherical particles (e.g., capsids) passing through a circular pore.

SUMMARY POINTS

1. Advances in fabrication techniques enhance opportunities to explore phenomena that occur at nanometer dimensions. Forming nanochannels in a planar format permits simultaneous optical imaging and electrical measurements, whereas integration of nanopores with microfluidic devices forms an out-of-plane structure that permits multilayer analysis.

2. Ion-current rectification occurs in nanochannels that have a geometrical or surface-charge asymmetry, and the degree of rectification is controlled by ionic strength, buffer pH, lateral dimensions, geometry, and surface modification.
3. Concentration polarization produces ion enrichment, ion depletion, and sample stacking at the interface between micro- and nanochannels. These phenomena allow efficient sample concentration to be achieved in short periods of time.
4. Formation of nanochannels with heterogeneous materials or surface modifications allows precise manipulation of fluid and ion transport. Fluidic diodes and transistors are constructed with these techniques.
5. Biological, solid-state, and synthetic pores are used to characterize various analytes, including DNA, viruses, proteins, polymers, small molecules, nanoparticles, and metal ions.

FUTURE ISSUES

1. An improved understanding of ion-transport mechanisms, especially ion-current rectification, in nanofluidic channels is an important next step. These efforts will require extensive modeling backed by appropriate experiments.
2. More complex micro- and nanofluidic circuits will be designed, modeled, fabricated, and tested to characterize individual and ensembles of molecules and particles.
3. Resistive-pulse sensing will be improved (*a*) by multiple interrogations of a single analyte to increase measurement precision and (*b*) through parallel analyses of multiple analytes to enhance throughput and detection limits.

DISCLOSURE STATEMENT

The authors receive funding to conduct nanofluidics-based research.

ACKNOWLEDGMENTS

This work was supported in part by National Science Foundation grants CHE-0750295 and CHE-0832651.

LITERATURE CITED

1. Kovarik ML, Jacobson SC. 2009. Nanofluidics in lab-on-a-chip devices. *Anal. Chem.* 81:7133–40
2. Bayley H, Cremer PS. 2001. Stochastic sensors inspired by biology. *Nature* 413:226–30
3. Li J, Stein D, McMullan C, Branton D, Aziz MJ, Golovchenko JA. 2001. Ion-beam sculpting at nanometre length scales. *Nature* 412:166–69
4. Uram JD, Ke K, Hunt AJ, Mayer M. 2006. Submicrometer pore-based characterization and quantification of antibody–virus interactions. *Small* 2:967–72
5. Storm AJ, Chen J, Ling X, Zandbergen HW, Dekker C. 2003. Fabrication of solid-state nanopores with single-nanometre precision. *Nat. Mater.* 2:537–40
6. Wei C, Bard AJ, Feldberg SW. 1997. Current rectification at quartz nanopipet electrodes. *Anal. Chem.* 69:4627–33

7. DeBlois RW, Bean CP. 1970. Counting and sizing of submicron particles by resistive pulse technique. *Rev. Sci. Instrum.* 41:909–16
8. Merchant CA, Healy K, Wanunu M, Ray V, Peterman N, et al. 2010. DNA translocation through graphene nanopores. *Nano Lett.* 10:2915–21
9. Schneider GF, Kowalczyk SW, Calado VE, Pandraud G, Zandbergen HW, et al. 2010. DNA translocation through graphene nanopores. *Nano Lett.* 10:3163–67
10. Zhou K, Kovarik ML, Jacobson SC. 2008. Surface-charge induced ion depletion and sample stacking near single nanopores in microfluidic devices. *J. Am. Chem. Soc.* 130:8614–16
11. Kovarik ML, Jacobson SC. 2008. Integrated nanopore/microchannel devices for AC electrokinetic trapping of particles. *Anal. Chem.* 80:657–64
12. Cannon DM, Kuo T-C, Bohn PW, Sweedler JV. 2003. Nanocapillary array interconnects for gated analyte injections and electrophoretic separations in multilayer microfluidic architectures. *Anal. Chem.* 75:2224–30
13. Kuo T-C, Cannon DM, Chen YN, Tulock JJ, Shannon MA, et al. 2003. Gateable nanofluidic interconnects for multilayered microfluidic separation systems. *Anal. Chem.* 75:1861–67
14. Karnik R, Castelino K, Fan R, Yang P, Majumdar A. 2005. Effects of biological reactions and modifications on conductance of nanofluidic channels. *Nano Lett.* 5:1638–42
15. Umehara S, Pourmand N, Webb CD, Davis RW, Yasuda K, Karhanek M. 2006. Current rectification with poly-L-lysine-coated quartz nanopipettes. *Nano Lett.* 6:2486–92
16. Fu J, Schoch RB, Stevens AL, Tannenbaum SR, Han J. 2007. A patterned anisotropic nanofluidic sieving structure for continuous-flow separation of DNA and proteins. *Nat. Nanotechnol.* 2:121–28
17. Kovarik ML, Jacobson SC. 2007. Attoliter-scale dispensing in nanofluidic channels. *Anal. Chem.* 79:1655–60
18. Perry JM, Zhou K, Harms ZD, Jacobson SC. 2010. Ion transport in nanofluidic funnels. *Am. Chem. Soc. Nano* 4:3897–902
19. Nam SW, Lee MH, Lee SH, Lee DJ, Rossnagel SM, Kim KB. 2010. Sub-10-nm nanochannels by self-sealing and self-limiting atomic layer deposition. *Nano Lett.* 10:3324–29
20. Lee JH, Chung S, Kim SJ, Han J. 2007. Poly(dimethylsiloxane)-based protein preconcentration using a nanogap generated by junction gap breakdown. *Anal. Chem.* 79:6868–73
21. Höltzel A, Tallarek U. 2007. Ionic conductance of nanopores in microscale analysis systems: where microfluidics meets nanofluidics. *J. Sep. Sci.* 30:1398–419
22. Schoch RB, Han J, Renaud P. 2008. Transport phenomena in nanofluidics. *Rev. Mod. Phys.* 80:839–83
23. Karnik R, Duan C, Castelino K, Daiguji H, Majumdar A. 2007. Rectification of ionic current in a nanofluidic diode. *Nano Lett.* 7:547–51
24. Siwy Z, Fulinski A. 2002. Fabrication of a synthetic nanopore ion pump. *Phys. Rev. Lett.* 89:198103
25. Cervera J, Schiedt B, Neumann R, Mafe S, Ramirez P. 2006. Ionic conduction, rectification, and selectivity in single conical nanopores. *J. Chem. Phys.* 124:104706
26. Stein D, Kruithof M, Dekker C. 2004. Surface-charge-governed ion transport in nanofluidic channels. *Phys. Rev. Lett.* 93:035901
27. Kovarik ML, Zhou K, Jacobson SC. 2009. Effect of conical nanopore diameter on ion current rectification. *J. Phys. Chem. B* 113:15960–66
28. Siwy Z, Heins E, Harrell CC, Kohli P, Martin CR. 2004. Conical-nanotube ion-current rectifiers: the role of surface charge. *J. Am. Chem. Soc.* 126:10850–51
29. Siwy Z, Apel P, Dobrev D, Neumann R, Spohr R, et al. 2003. Ion transport through asymmetric nanopores prepared by ion track etching. *Nucl. Instrum. Methods Phys. Res. Sect. B* 208:143–48
30. Ermakova LE, Sidorova MP, Bezrukova ME. 1998. Filtration and electrokinetic characteristics of track membranes. *Colloid J.* 60:705–12
31. Jung J-Y, Joshi P, Petrossian L, Thornton TJ, Posner JD. 2009. Electromigration current rectification in a cylindrical nanopore due to asymmetric concentration polarization. *Anal. Chem.* 81:3128–33
32. Wang J, Martin CR. 2008. A new drug-sensing paradigm based on ion-current rectification in a conically shaped nanopore. *Nanomedicine* 3:13–20
33. White HS, Bund A. 2008. Ion current rectification at nanopores in glass membranes. *Langmuir* 24:2212–18

34. Siwy ZS. 2006. Ion-current rectification in nanopores and nanotubes with broken symmetry. *Adv. Funct. Mater.* 16:735–46
35. Cervera J, Schiedt B, Ramirez P. 2005. A Poisson/Nernst-Planck model for ionic transport through synthetic conical nanopores. *Euro. Phys. Lett.* 71:35–41
36. Liu Q, Wang Y, Guo W, Ji H, Xue J, Ouyang Q. 2007. Asymmetric properties of ion transport in a charged conical nanopore. *Phys. Rev. E* 75:051201
37. Woermann D. 2002. Analysis of non-ohmic electrical current–voltage characteristic of membranes carrying a single track-etched conical pore. *Nucl. Instrum. Methods Phys. Res. Sect. B* 194:458–62
38. Qian S, Joo SW, Ai Y, Cheney MA, Hou W. 2009. Effect of linear surface-charge non-uniformities on the electrokinetic ionic-current rectification in conical nanopores. *J. Colloid Interface Sci.* 329:376–83
39. Ramirez P, Apel PY, Cervera J, Mafe S. 2008. Pore structure and function of synthetic nanopores with fixed charges: tip shape and rectification properties. *Nanotechnology* 19:315707
40. Yusko EC, An R, Mayer M. 2010. Electroosmotic flow can generate ion current rectification in nano- and micropores. *Am. Chem. Soc. Nano* 4:477–87
41. Ai Y, Zhang M, Joo SW, Cheney MA, Qian S. 2010. Effects of electroosmotic flow on ionic current rectification in conical nanopores. *J. Phys. Chem. C* 114:3883–90
42. Siwy Z, Kosinska ID, Fulinski A, Martin CR. 2005. Asymmetric diffusion through synthetic nanopores. *Phys. Rev. Lett.* 94:048102
43. Pu Q, Yun J, Temkin H, Liu S. 2004. Ion-enrichment and ion-depletion effect of nanochannel structures. *Nano Lett.* 4:1099–103
44. Kim SJ, Wang YC, Lee JH, Jang H, Han J. 2007. Concentration polarization and nonlinear electrokinetic flow near a nanofluidic channel. *Phys. Rev. Lett.* 99:044501
45. Zangle TA, Mani A, Santiago JG. 2010. Effects of constant voltage on time evolution of propagating concentration polarization. *Anal. Chem.* 82:3114–17
46. Wang Y-C, Stevens AL, Han J. 2005. Million-fold preconcentration of proteins and peptides by nanofluidic filter. *Anal. Chem.* 77:4293–99
47. Wang Y-C, Han J. 2008. Pre-binding dynamic range and sensitivity enhancement for immuno-sensors using nanofluidic preconcentrator. *Lab Chip* 8:392–94
48. Laws DR, Hlushkou D, Perdue RK, Tallarek U, Crooks RM. 2009. Bipolar electrode focusing: simultaneous concentration enrichment and separation in a microfluidic channel containing a bipolar electrode. *Anal. Chem.* 81:8923–29
49. Kim SJ, Ko SH, Kang KH, Han J. 2010. Direct seawater desalination by ion concentration polarization. *Nat. Nanotechnol.* 5:297–301
50. Harrell CC, Kohli P, Siwy Z, Martin CR. 2004. DNA-nanotube artificial ion channels. *J. Am. Chem. Soc.* 126:15646–47
51. Yameen B, Ali M, Neumann R, Ensinger W, Knoll W, Azzaroni O. 2009. Single conical nanopores displaying pH-tunable rectifying characteristics. Manipulating ionic transport with zwitterionic polymer brushes. *J. Am. Chem. Soc.* 131:2070–71
52. Yameen B, Ali M, Neumann R, Ensinger W, Knoll W, Azzaroni O. 2009. Synthetic proton-gated ion channels via single solid-state nanochannels modified with responsive polymer brushes. *Nano Lett.* 9:2788–93
53. Karnik R, Castelino K, Duan C, Majumdar A. 2006. Diffusion-limited patterning of molecules in nanofluidic channels. *Nano Lett.* 6:1735–40
54. Vlassiouk I, Siwy ZS. 2007. Nanofluidic diode. *Nano Lett.* 7:552–56
55. Yan R, Liang W, Fan R, Yang P. 2009. Nanofluidic diodes based on nanotube heterojunctions. *Nano Lett.* 9:3820–25
56. Karnik R, Fan R, Yue M, Li D, Yang P, Majumdar A. 2005. Electrostatic control of ions and molecules in nanofluidic transistors. *Nano Lett.* 5:943–48
57. Karnik R, Castelino K, Majumdar A. 2006. Field-effect control of protein transport in a nanofluidic transistor circuit. *Appl. Phys. Lett.* 88:123114
58. Macrae MX, Blake S, Mayer M, Yang J. 2010. Nanoscale ionic diodes with tunable and switchable rectifying behavior. *J. Am. Chem. Soc.* 132:1766–67

59. Daiguji H, Oka Y, Shirono K. 2005. Nanofluidic diode and bipolar transistor. *Nano Lett.* 5:2274–80
60. Oh YJ, Garcia AL, Petsev DN, Lopez GP, Brueck SRJ, et al. 2009. Effect of wall-molecule interactions on electrokinetic transport of charged molecules in nanofluidic channels during FET flow control. *Lab Chip* 9:1601–8
61. Vermesh U, Choi JW, Vermesh O, Fan R, Nagarah J, Heath JR. 2009. Fast nonlinear ion transport via field-induced hydrodynamic slip in sub-20-nm hydrophilic nanofluidic transistors. *Nano Lett.* 9:1315–19
62. Nam SW, Rooks MJ, Kim KB, Rossnagel SM. 2009. Ionic field effect transistors with sub-10-nm multiple nanopores. *Nano Lett.* 9:2044–48
63. Ogston AG. 1958. The spaces in a uniform random suspension of fibres. *Trans. Faraday Soc.* 54:1754–57
64. Cabodi M, Turner SWP, Craighead HG. 2002. Entropic recoil separation of long DNA molecules. *Anal. Chem.* 74:5169–74
65. Han J, Craighead HG. 2000. Separation of long DNA molecules in a microfabricated entropic trap array. *Science* 288:1026–29
66. Han J, Craighead HG. 2002. Characterization and optimization of an entropic trap for DNA separation. *Anal. Chem.* 74:394–401
67. Han J, Turner SW, Craighead HG. 1999. Entropic trapping and escape of long DNA molecules at submicron size constriction. *Phys. Rev. Lett.* 83:1688–91
68. Martin CR, Siwy ZS. 2007. Learning nature's way: biosensing with synthetic nanopores. *Science* 317:331–32
69. Branton D, Deamer DW, Marziali A, Bayley H, Benner SA, et al. 2008. The potential and challenges of nanopore sequencing. *Nat. Biotechnol.* 26:1146–53
70. Bezrukov SM, Vodyanoy I, Parsegian VA. 1994. Counting polymers moving through a single-ion channel. *Nature* 370:279–81
71. Song L, Hobaugh MR, Shustak C, Cheley S, Bayley H, Gouaux JE. 1996. Structure of staphylococcal α-hemolysin, a heptameric transmembrane pore. *Science* 274:1859–66
72. Kasianowicz JJ, Brandin E, Branton D, Deamer DW. 1996. Characterization of individual polynucleotide molecules using a membrane channel. *Proc. Natl. Acad. Sci. USA* 93:13770–73
73. Gu L-Q, Braha O, Conlan S, Cheley S, Bayley H. 1999. Stochastic sensing of organic analytes by a pore-forming protein containing a molecular adapter. *Nature* 398:686–90
74. Braha O, Gu L-Q, Zhou L, Lu X, Cheley S, Bayley H. 2000. Simultaneous stochastic sensing of divalent metal ions. *Nat. Biotechnol.* 18:1005–7
75. White RJ, Ervin EN, Yang T, Chen X, Daniel S, et al. 2007. Single ion-channel recordings using glass nanopore membranes. *J. Am. Chem. Soc.* 129:11766–75
76. Ervin EN, White RJ, White HS. 2009. Sensitivity and signal complexity as a function of the number of ion channels in a stochastic sensor. *Anal. Chem.* 81:533–37
77. Schibel AEP, Edwards T, Kawano R, Lan W, White HS. 2010. Quartz nanopore membranes for suspended bilayer ion channel recordings. *Anal. Chem.* 82:7259–66
78. Dekker C. 2007. Solid-state nanopores. *Nat. Nanotechnol.* 2:209–15
79. Li J, Gershow M, Stein D, Brandin E, Golovchenko JA. 2003. DNA molecules and configurations in a solid-state nanopore microscope. *Nat. Mater.* 2:611–15
80. Fologea D, Gershow M, Ledden B, McNabb DS, Golovchenko JA, Li J. 2005. Detecting single stranded DNA with a solid state nanopore. *Nano Lett.* 5:1905–9
81. Skinner GM, Van Den Hout M, Broekmans O, Dekker C, Dekker NH. 2009. Distinguishing single- and double-stranded nucleic acid molecules using solid-state nanopores. *Nano Lett.* 9:2953–60
82. Smeets RMM, Kowalczyk SW, Hall AR, Dekker NH, Dekker C. 2009. Translocation of RecA-coated double-stranded DNA through solid-state nanopores. *Nano Lett.* 9:3089–95
83. Kowalczyk SW, Hall AR, Dekker C. 2010. Detection of local protein structures along DNA using solid-state nanopores. *Nano Lett.* 10:324–28
84. Singer A, Wanunu M, Morrison W, Kuhn H, Frank-Kamenetskii M, Meller A. 2010. Nanopore based sequence specific detection of duplex DNA for genomic profiling. *Nano Lett.* 10:738–42
85. Wanunu M, Sutin J, Meller A. 2009. DNA profiling using solid-state nanopores: detection of DNA-binding molecules. *Nano Lett.* 9:3498–502

86. Garaj S, Hubbard W, Reina A, Kong J, Branton D, Golovchenko JA. 2010. Graphene as a subnanometre trans-electrode membrane. *Nature* 467:190–93
87. Heins EA, Siwy ZS, Baker LA, Martin CR. 2005. Detecting single porphyrin molecules in a conically shaped synthetic nanopore. *Nano Lett.* 5:1824–29
88. Harrell CC, Choi Y, Horne LP, Baker LA, Siwy ZS, Martin CR. 2006. Resistive-pulse DNA detection with a conical nanopore sensor. *Langmuir* 22:10837–43
89. Menon VP, Martin CR. 1995. Fabrication and evaluation of nanoelectrode ensembles. *Anal. Chem.* 67:1920–28
90. Siwy Z, Trofin L, Kohli P, Baker LA, Trautmann C, Martin CR. 2005. Protein biosensors based on biofunctionalized conical gold nanotubes. *J. Am. Chem. Soc.* 127:5000–1
91. Sexton LT, Horne LP, Sherrill SA, Bishop GW, Baker LA, Martin CR. 2007. Resistive-pulse studies of proteins and protein/antibody complexes using a conical nanotube sensor. *J. Am. Chem. Soc.* 129:13144–52
92. Wharton JE, Jin P, Sexton LT, Horne LP, Sherrill SA, et al. 2007. A method for reproducibly preparing synthetic nanopores for resistive-pulse biosensors. *Small* 3:1424–30
93. DeBlois RW, Bean CP, Wesley RKA. 1977. Electrokinetic measurements with submicron particles and pores by resistive pulse technique. *J. Colloid Interface Sci.* 61:323–35
94. Uram JD, Ke K, Hunt AJ, Mayer M. 2006. Label-free affinity assays by rapid detection of immune complexes in submicrometer pores. *Angew. Chem. Int. Ed.* 45:2281–85
95. Zhou K, Li L, Tan Z, Zlotnick A, Jacobson SC. 2010. Characterization of hepatitis B virus capsids by resistive-pulse sensing. *J. Am. Chem. Soc.* 133:1618–21
96. Kowalczyk SW, Tuijtel MW, Donkers SP, Dekker C. 2010. Unraveling single-stranded DNA in a solid-state nanopore. *Nano Lett.* 10:1414–20

Annual Review of
Analytical Chemistry

Volume 4, 2011

Contents

Indexes

Errata

An online log of corrections to the *Annual Review of Analytical Chemistry* articles may be found at http://arjournals.annualreviews.org/errata/anchem